Conical diffraction intensity profiles generated using a top-hat input beam

R. T. Darcy,[*] **D. McCloskey, K. E. Ballantine, J. G. Lunney,**
P. R. Eastham, and J. F. Donegan

AMBER & CRANN, School of Physics, Trinity College Dublin, Ireland

[*]*rdarcy@tcd.ie*

Abstract: The phenomenon of internal conical diffraction has been studied extensively for the case of laser beams with Gaussian intensity profiles incident along an optic axis of a biaxial material. This work presents experimental images for a top-hat input beam and offers a theoretical model which successfully describes the conically diffracted intensity profile, which is observed to differ qualitatively from the Gaussian case. The far-field evolution of the beam is predicted to be particularly interesting with a very intricate structure, and this is confirmed experimentally.

© 2014 Optical Society of America

OCIS codes: (260.1180) Crystal optics; (050.1940) Diffraction.

References and links

1. W. R. Hamilton, "Third supplement to an essay on the theory of systems of rays," Trans. R. Irish Acad. **17**, 137–139 (1837).
2. A. M. Belsky and A. P. Khapalyuk, "Internal conical refraction of bounded light beams in biaxial crystals," Opt. Spectrosc. **44**, 746–751 (1978).
3. M. V. Berry, "Conical diffraction asymptotics: fine structure of the Poggendorff rings and axial spike," J. Opt. A, Pure Appl. Opt. **6**(4), 289–300 (2004).
4. M. V. Berry, M. R. Jeffrey, and J. G. Lunney, "Conical diffraction: observations and theory," Proc. R. Soc. A **462**, 1629–1642 (2006).
5. C. F. Phelan, D. P. O'Dwyer, Y. P. Rakovich, J. F. Donegan, and J. G. Lunney, "Conical diffraction and Bessel beam formation with a high optical quality biaxial crystal," Opt. Express **17**(15), 12891–12899 (2009).
6. C. F. Phelan, K. E. Ballantine, P. R. Eastham, J. F. Donegan, and J. G. Lunney, "Conical diffraction of a Gaussian beam with a two crystal cascade," Opt. Express **20**(12), 13201–13207 (2012).
7. D. P. O'Dwyer, C. F. Phelan, Y. P. Rakovich, P. R. Eastham, J. G. Lunney, and J. F. Donegan, "The creation and annihilation of optical vortices using cascade conical diffraction," Opt. Express **19**(3), 2580–2588 (2011).
8. R. T. Darcy, D. McCloskey, K. E. Ballantine, B. D. Jennings, J. G. Lunney, P. R. Eastham, and J. F. Donegan, "White light conical diffraction," Opt. Express **21**(17), 20394–20403 (2013).
9. D. P. O'Dwyer, C. F. Phelan, K. E. Ballantine, Y. P. Rakovich, J. G. Lunney, and J. F. Donegan, "Conical diffraction of linearly polarised light controls the angular position of a microscopic object," Opt. Express **18**(26), 27319–27326 (2010).
10. A. Turpin, V. Shvedov, C. Hnatovsky, Y. V. Loiko, J. Mompart, and W. Krolikowski, "Optical vault: A reconfigurable bottle beam based on conical refraction of light," Opt. Express **21**(22), 26335–26340 (2013).
11. M. Born and E. Wolf, *Principles of Optics* (Cambridge University, 1999).
12. L. D. Landau, E. M. Lifshitz, and L. P. Pitaevskii, *Electrodynamics of Continuous Media* (Pergamon, 1984).
13. M. V. Berry and M. R.Jeffrey, "Hamilton's diabolical point at the heart of crystal optics," Prog. Opt. **50**, 13–50 (2007).
14. M. C. Pujol, M. Rico, C. Zaldo, R. Solé, V. Nikolov, X. Solans, M. Aguiló, and F. Díaz, "Crystalline structure and optical spectroscopy of Er^{3+}-doped $KGd(WO_4)_2$ single crystals," Appl. Phys. B **68**, 187–197 (1999).
15. M. R. Jeffrey, *Conical Diffraction: Complexifying Hamilton's Diabolical Legacy* (University of Bristol, 2007).
16. V. Peet, "The far-field structure of Gaussian light beams transformed by internal conical refraction in a biaxial crystal," Opt. Commun. **311**, 150–155 (2013).
17. M. V. Berry, "Exact nonparaxial transmission of subwavelength detail using superoscillations," J. Phys. A: Math. Theor. **46**, 205203 (2013).

18. A. Ashkin, *Optical Trapping and Manipulation of Neutral Particles Using Lasers* (World Scientific, 2007).
19. M. V. Berry, "Conical diffraction from an *N*-crystal cascade," J. Opt. **12**, 75704–75712 (2010).
20. T. A. King, W. Hogervorst, N. S. Kazak, N. A. Khilo, and A. A. Ryzhevich, "Formation of higher-order Bessel light beams in biaxial crystals," Opt. Commun. **187**, 407–414 (2001).

1. Introduction

Conical diffraction was first predicted by William Rowan Hamilton of Trinity College Dublin in 1882 [1]. As part of his extensive work on mathematical optics, he predicted that a light ray incident along an optic axis of a biaxial medium would be transformed into a hollow cone of light inside the material. If the material was cut such that the entrance and exit faces were parallel to each other and orthogonal to an optic axis, then the light would emerge as a hollow cylinder. This prediction was experimentally confirmed later that year by Humphrey Lloyd using the biaxial material arragonite. Hamilton's consideration was that of a refractive phenomenon and led to the term 'conical refraction'. It was not until the development of the theory by Belsky and Khapalyuk [2], which considered diffraction in a paraxial wave-theory model, that the nomenclature was switched to 'conical diffraction'. This model was later reformulated by Berry [3] and remains a highly accurate description of the phenomenon; notably present in the model is the Poggendorff dark ring, a narrow region of zero intensity between two bright rings, which is absent from Hamilton's treatment. It is for this reason that we will refer to the phenomenon as 'conical diffraction'.

Conical diffraction has been extensively studied using an input laser beam [4–7]. Such beams are approximately Gaussian, and so the models describing conical diffraction often assume an input Gaussian beam. Even in cases where broad sources were used to produce the phenomenon, it was important to use a spatial filter to form a spatially coherent beam which was approximately Gaussian in the focal image plane in order for the established theory to remain valid [8]. In this paper we consider another type of input beam, namely a 'top-hat' beam, and demonstrate how it exhibits interesting intensity profiles beyond the crystal with a rich beam evolution structure. Although the first observation of conical diffraction by Lloyd used a pinhole in front of arragonite, thus resulting in a top-hat beam, since then it appears no experimental images have been produced with this beam profile. We present experimental images of conically diffracted beams produced using a top-hat source which are qualitatively different from those produced using a Gaussian source, in particular featuring a narrow ring of high intensity and a wedge-shaped structure with a rapid drop in intensity at the beam edge. This novel and unusual beam shape could find applications in areas such as optical trapping [9, 10], laser etching, and high NA direct write photolithography.

2. Theory

Conical diffraction is an optical phenomenon observed in biaxial materials, which have three principal refractive indices $n_1 < n_2 < n_3$. Light incident along one of the two optic axes in such a material undergoes internal conical diffraction and spreads out as a hollow cone with semi angle

$$A = \tfrac{1}{2} \arctan \left[n_2^2 \sqrt{\left(n_1^{-2} - n_2^{-2} \right) \left(n_2^{-2} - n_3^{-2} \right)} \right]. \tag{1}$$

The geometrical optics description of this may be found in [11] and [12]. For many biaxial materials A is small, on the order of 10^{-2} rad, and hence a paraxial approximation may be used to determine the radius of the ring of light as it emerges from such a material of length l:

$$R_0 = \frac{l}{2} \frac{\sin(2A)}{\cos(2A)} = \frac{l}{2} \tan(2A) \approx Al. \tag{2}$$

A rigorous examination of the validity of this paraxial approximation when modelling conical diffraction is shown in [13]. The biaxial material used in the experiments presented in this paper is KGd(WO$_4$)$_2$ whose principal refractive indices have been determined by Pujol *et al.* [14]. For light at 632.8 nm the values are calculated to be $n_1 = 2.0109$, $n_2 = 2.0414$, and $n_3 = 2.0950$.

In order to develop a theory which describes conical diffraction it is useful to first define some dimensionless beam parameters following the notation used by Berry and Jeffrey [13]:

$$\rho_0 \equiv \frac{Al}{w} = \frac{R_0}{w}, \qquad \rho \equiv \frac{R}{w}, \qquad \zeta \equiv \frac{l + (z-l)n_2}{n_2 k_0 w^2} = \frac{Z}{n_2 k_0 w^2}, \qquad (3)$$

where $k_0 = 2\pi/\lambda$, R is measured along the radius of the beam with $R = 0$ at the centre of the beam, and z is measured along the propagation direction of the beam with $z = 0$ at the location of the focused image of the source in the absence of the crystal. The terms in these equations may be seen in Fig. 1. While these parameters are defined for Gaussian beams with a $1/e$ intensity radius of w, they are also useful for top-hat beams where w has been defined to be the radius of the beam. When $\zeta = 0$ the conically diffracted rings are most sharply defined and this location is known as the focal image plane (FIP). Letting $\zeta = 0$ in Eq. (3) yields the location z_{FIP} of the FIP measured from $z = 0$:
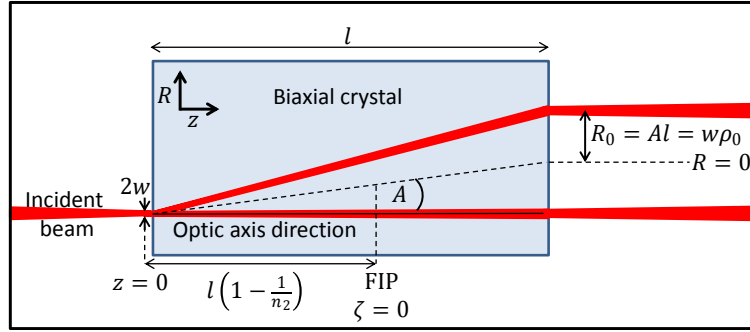
$$z_{\text{FIP}} = l(1 - 1/n_2). \qquad (4)$$

Fig. 1. A light beam undergoing conical diffraction within a biaxial material. This diagram is a two-dimensional slice taken along the plane where $R = 0$.

When a beam with electric displacement field profile $D_0(\rho)$ enters a biaxial material along the optic axis it is conically diffracted. If the beam is radially symmetric and circularly polarised (or unpolarised), the equations describing this transformation are [3]

$$B_0(\rho, \rho_0, \zeta) = \int_0^\infty d\kappa\, \kappa\, a(\kappa) \exp\left(-\tfrac{1}{2} i\zeta\kappa^2\right) J_0(\kappa\rho) \cos(\kappa\rho_0), \qquad (5)$$

$$B_1(\rho, \rho_0, \zeta) = \int_0^\infty d\kappa\, \kappa\, a(\kappa) \exp\left(-\tfrac{1}{2} i\zeta\kappa^2\right) J_1(\kappa\rho) \sin(\kappa\rho_0), \qquad (6)$$

where $J_\nu(x)$ is the νth order Bessel function of the first kind and $a(\kappa)$ is the Fourier transform of the input profile $D_0(\rho)$ given by

$$a(\kappa) = \int_0^\infty d\rho\, \rho D_0(\rho) J_0(\kappa\rho). \qquad (7)$$

The intensity distribution after the crystal is then given by [3]

$$I(\rho,\rho_0,\zeta) = |B_0(\rho,\rho_0,\zeta)|^2 + |B_1(\rho,\rho_0,\zeta)|^2. \tag{8}$$

The electric displacement field profile of a Gaussian beam can be expressed, in terms of the beam parameters shown in Eq. (3), as

$$D_{0G}(\rho) = \exp\left(-\rho^2/2\right). \tag{9}$$

The corresponding intensity profile is plotted in Fig. 2(a). Using Eq. (7) the Fourier transform of a Gaussian beam is

$$a_G(\kappa) = \exp\left(-\kappa^2/2\right). \tag{10}$$

Top-hat beam electric displacement field profiles are given by

$$D_{0T}(\rho) = \Theta(1-\rho), \tag{11}$$

where $\Theta(x)$ is the unit step function defined by

$$\Theta(x) \equiv \begin{cases} 0, & x < 0 \\ 1, & x \geq 0 \end{cases}. \tag{12}$$

The top-hat intensity profile is plotted in Fig. 2(b). The corresponding Fourier transform of a top-hat beam is then obtained using Eq. (7):

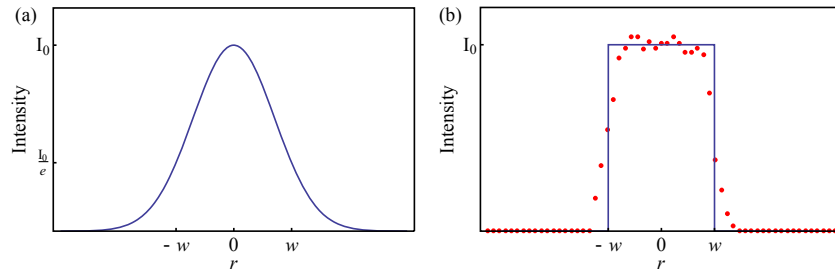$$a_T(\kappa) = J_1(\kappa)/\kappa. \tag{13}$$

Fig. 2. Plot (a) is a Gaussian intensity profile calculated using the electric displacement field given by Eq. (9). The value w is the $1/e$ radius of the beam. Plot (b) shows a top-hat profile calculated using the electric displacement field given by Eq. (11). The red dots in (b) show a profile, taken from an experimental image, of the beam used in the experiments which demonstrates a reasonably good approximation of a top-hat beam.

The Fourier transforms of the two input profiles given by Eqs. (10) and (13) may now be substituted in Eqs. (5) and (6) to give the intensity profiles in the focal image plane using Eq. (8) with $\zeta = 0$. These profiles are plotted in Fig. 3. The use of a top-hat input beam is predicted to produce a strikingly different profile from the case of using a Gaussian input beam. Most notable in Fig. 3(b) is the presence of a singularity and a wedge-shaped feature with an instantaneous diminution, as predicted by Berry [3].
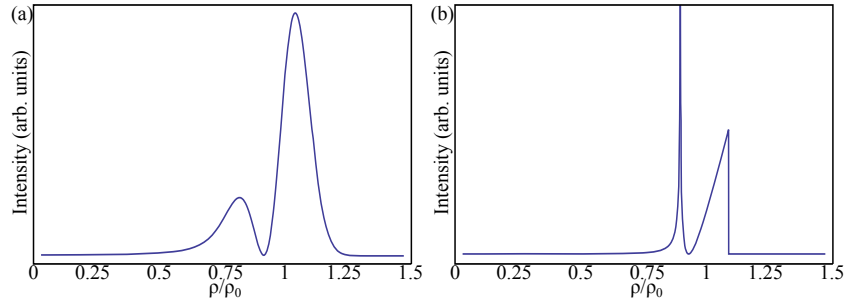
Fig. 3. Intensity profiles at the FIP generated using Eq. (8) in the case of (a) a Gaussian input beam, as given by Eq. (9), and (b) a top-hat input beam, as given by Eq. (11).

3. Fine structure of the radial intensity profile at the FIP

The intriguing intensity profile predicted to occur for a top-hat input beam as seen in Fig. 3(b) merits closer examination. The singularity cannot of course be infinite in reality, but what we actually observe is still of interest and should be quantified. In order to study this profile in fine detail the experimental apparatus shown in Fig. 4 was used. A Helium-Neon (HeNe) laser beam with a peak emission at 632.8 nm was directed onto a 100 μm diameter pinhole. Since the radius of the laser beam was of the order of millimetres, the 100 μm pinhole acted to cut off enough of the beam to generate a top-hat profile. A 22 mm long slab of $KGd(WO_4)_2$ was placed as close as possible to the pinhole and the crystal was aligned so that the beam propagated along an optic axis. A biconvex lens of focal length $f = 3$ cm was placed $u = 3.11$ cm after the FIP where $\zeta = 0$. This location occurs inside the crystal as can be found using Eq. (4). The image of the FIP was formed 86 cm after the lens, where a colour charge-coupled device (CCD) of pixel size 4.65 μm was placed to record the profiles generated. The magnification produced by the lens was calculated to be $m = |v/u| = 28$ which was sufficient to almost fill the CCD chip with the entire singularity and wedge structure. The unmagnified FIP radius was determined to be $R_0 = 360 \pm 10$ μm which corresponds to $\rho_0 = 7.2$ when using a pinhole with a 50 μm radius. Note that this value differs from the predicted value of $R_0 = 430$ μm obtained using Eq. (2), a discrepancy which is discussed in more detail in [8].
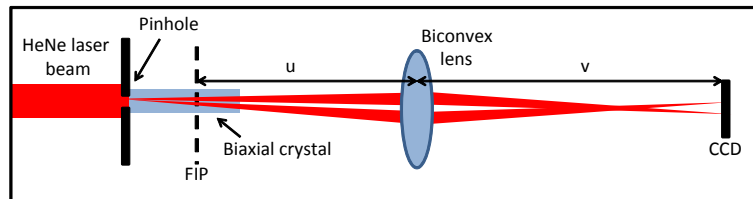

Fig. 4. The experimental setup used to study the fine structure of the beam profile in the FIP which is imaged onto the CCD. The values of u and v can be adjusted independently to give the image a desired magnification.

An example of the images recorded using this apparatus is shown in Fig. 5. Both images are taken at the FIP, with Fig. 5(b) demonstrating the observed profile when using a top-hat input beam. Figure 5(a) is an image generated using a Gaussian input beam as reported by Darcy *et al.* [8].
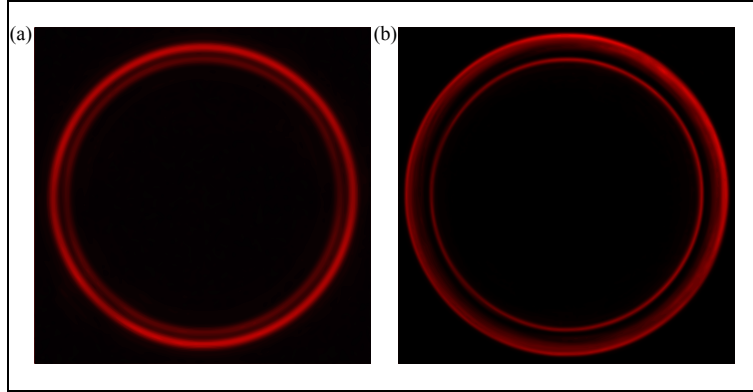
Fig. 5. (a) An experimental image of the conically diffracted Gaussian beam in the FIP. The structure is distinct from that formed when using a top-hat input beam as seen in (b). The radius of the Poggendorff dark ring in image (b) was determined to be 360 ± 10 μm. Both images are 0.8 mm $\times$ 0.8 mm.

In practice the range over which Eqs. (5) and (6) are integrated is not infinite, rather the experimental apparatus will introduce constraints on these values [15] with the maximum contribution κ_{max} being the maximum transverse wavevector component reaching the imaging device. Consider an iris of radius R_{lim} centred on the conically diffracted beam and placed a distance z_{iris} from the entrance face of the crystal, as seen in Fig. 6. The maximum transverse wavevector component κ_{max} passing through this iris is then

$$\kappa_{\mathrm{max}} \equiv n_2 k_0 w \sin \left[\arctan \left(\frac{R_{\mathrm{lim}}}{z_{\mathrm{iris}}} \right) \right]. \tag{14}$$
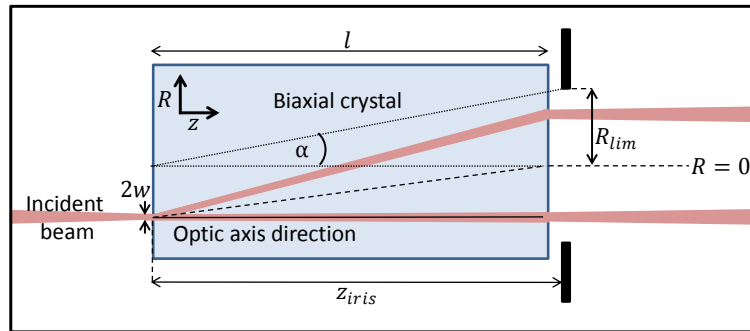

Fig. 6. The maximum transmissible transverse wavevector component κ_{max} is determined by the radius of the iris R_{lim} and its position z_{iris}. This transverse wavevector is given by $\kappa_{\mathrm{max}} = n_2 k_0 w \sin \alpha$ where $\alpha = \arctan (R_{\mathrm{lim}}/z_{\mathrm{iris}})$.

This is effectively a low-pass spatial filter effect, cutting off higher transverse wavevector components reaching the imaging device while retaining lower components. The smallest iris in the system shown in Fig. 4 is the crystal itself which has a limiting radius of $R_{\mathrm{lim}} = 1.5$ mm. Since the beam is free to propagate transversely in the crystal until it emerges, the value of z_{iris} is simply the length of the crystal, 22 mm. Using these values in Eq. (14) gives $\kappa_{\mathrm{max}} = 69$ which was subsequently used in Eq. (8) to generate the plot shown in Fig. 7(a). This is compared with

the observed intensity profile obtained by averaging several radial profiles and shows very good agreement. The rapid oscillations of the profile for $0.9 \leq \rho/\rho_0 \leq 1.1$ are somewhat smoothed out in the experimental profile due to the effect of this averaging.

A variable iris was then inserted between the crystal and the biconvex lens, a distance of $z_{iris} = 40$ mm from the entrance face of the crystal. When the iris was at its minimum setting, the limiting radius was $R_{lim} = 0.75$ mm which is smaller than the radius of the crystal, and so using Eq. (14) we find $\kappa_{max} = 19$. Equation (8) was subsequently used to calculate the theoretical intensity profile shown in Fig. 7(b), compared with the experimentally observed profile, again showing very good agreement. The inner ring is less intense than the case with no iris as seen in Fig. 7(a), and it is also broader. The oscillations of the wedge-shaped feature have become more pronounced with longer periods than in Fig. 7(a).
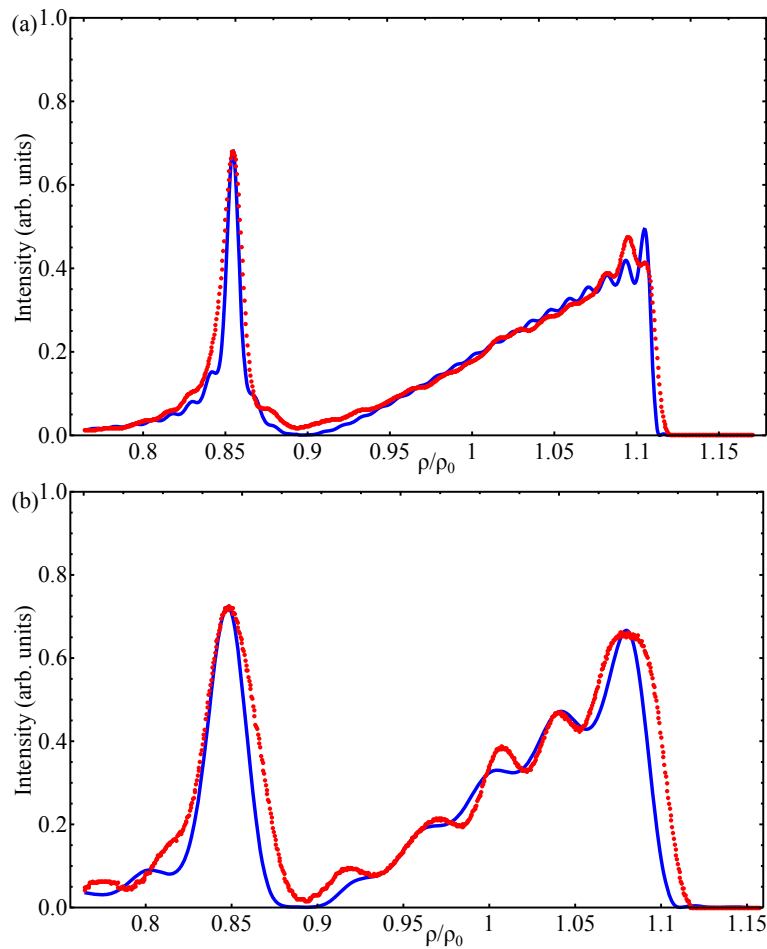

Fig. 7. (a) Comparison of the observed intensity profile (red dots) with the theoretical profile (solid blue) where $\kappa_{max} = 69$. (b) Comparison of the observed intensity profile (red dots) with the theoretical profile (solid blue) where $\kappa_{max} = 19$ corresponding to an iris of diameter 1.5 mm present before the imaging lens in Fig. 4.

4. Far-field propagation

The conically diffracted beam evolves as it propagates beyond the focal image plane. This evolution has been examined in the case of a Gaussian input profile [5, 16]. In this case the rings which form at the FIP spread out as ζ increases and eventually the inner ring converges to produce a high intensity region in the centre of the beam $\rho = 0$ known as the 'axial spike'. When $\rho_0 \gg 1$, the peak intensity of this axial spike occurs at $\zeta \approx \rho_0 \sqrt{2/3}$. A theoretical plot of the evolution over the range $0 \le \zeta \le 10$ is shown in Fig. 8 generated using Eq. (8) with $\rho_0 = 7.2$ and $a(\kappa)$ given by Eq. (10).
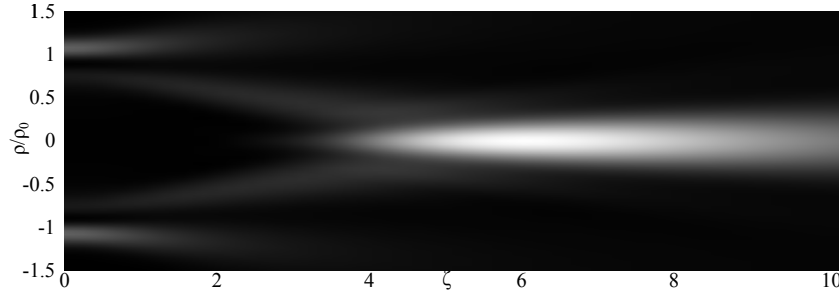

Fig. 8. Theoretical plot of the far-field evolution of a conically diffracted Gaussian beam generated using Eq. (8).

The propagation of a conically diffracted top-hat beam beyond the FIP was examined using the experimental arrangement in Fig. 9. A HeNe laser beam was directed onto a 100 μm diameter pinhole and a biconvex lens of focal length $f = 10$ cm was placed a distance $u = 20$ cm after the pinhole. This produced an unmagnified image of the pinhole a distance $v = 20$ cm after the lens. The profile of the laser beam at this point $z = 0$ approximated a top-hat very well as shown by the red dots in Fig. 2(b). When a 22 mm long slab of KGd(WO$_4$)$_2$ was inserted into the beam between the lens and $z = 0$, the FIP occurred outside the crystal as determined by Eq. (4). A CCD with a pixel size of 6 μm was mounted on a rail allowing movement in the ζ direction.
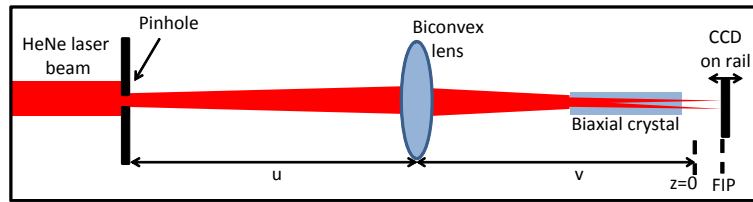

Fig. 9. The experimental setup used to study how the conically diffracted top-hat beam evolves in space. The pinhole is imaged using a biconvex lens of focal length f to a point $z = 0$ beyond the crystal, thus using Eq. (4) the FIP occurs outside the crystal at a distance $v + l(1 - 1/n_2)$ from the lens. z increases in the direction of beam propagation, and hence so do Z and ζ as given by Eq. (3).

The system was used to record a series of images beginning at $\zeta = 0$ and moving away from the crystal in 1 mm increments to $Z = 8$ cm corresponding to $\zeta = 2.8$. The images were then stitched together using numerical interpolation software which allowed the beam propagation to be viewed from the side. The resultant intensity profile is shown in Fig. 10(b). A theoretical profile was generated to show how the beam evolves in this region using Eq. (8) with $a(\kappa)$ given

by Eq. (13). The theoretical profile is shown in Fig. 10(a). There is good agreement between theory and experiment and the presence of the predicted oscillatory axial spike is obvious; a feature which does not occur for the Gaussian input beam as seen in Fig. 8.
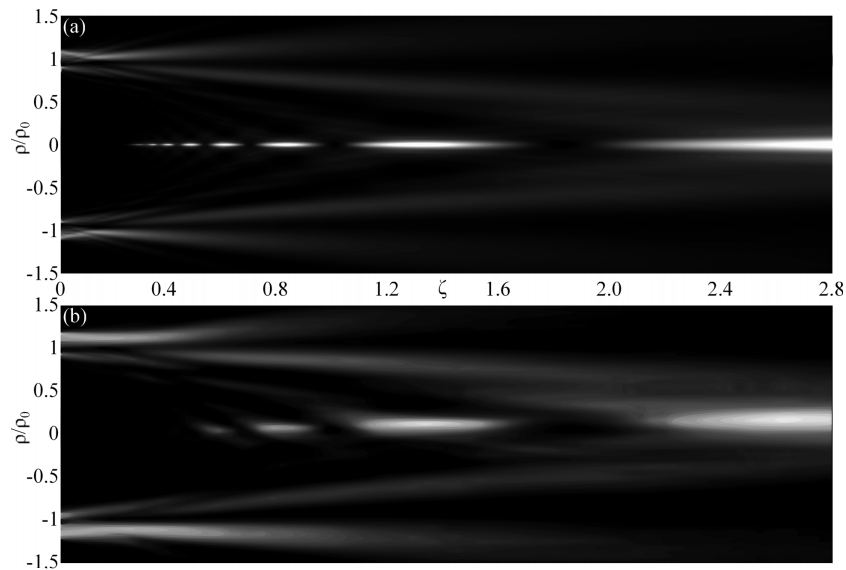

Fig. 10. Comparison of the theoretical evolution of the beam (a) with the observed evolution (b) in the case of a 50 μm radius top-hat beam. Image (b) was generated by stitching together a series of images taken at 1 mm increments in the direction of beam propagation.

The unusual structure of the evolution was examined more closely by generating a log plot of the intensity as shown in Fig. 11. It becomes apparent that the structure is very complex, with many rings of light which converge as the beam propagates. Indeed it appears that there are a multitude of intensity maxima where the rings converge along the $\rho = 0$ line for $0 < \zeta < 0.4$ which appear and disappear over extremely short distances.
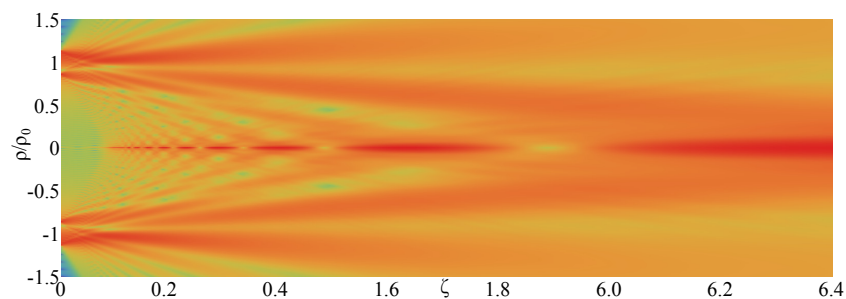

Fig. 11. A logarithmic plot of the far-field evolution of a conically diffracted top-hat beam, calculated using Eq. (8), in order to show the very complicated and intricate structure of the beam. It also demonstrates how the oscillating lobes along the $\rho = 0$ line are formed from many converging rings.

One may intuitively understand the presence of such converging rings to be a result of the diffraction of a top-hat beam as it propagates, giving rise to many fringes, as opposed to a Gaussian beam which remains Gaussian as it propagates. In order to explain the oscillatory

nature of the axial spike in a more rigorous way, we must use the following stationary phase approximation for the intensity of the conically diffracted beam at $\rho = 0$ taken from Jeffrey [15]:

$$I(\rho = 0, \zeta) \approx \frac{\pi \rho_0^2}{2\zeta^3} \left| a\left(\frac{\rho_0}{\zeta}\right) \right|^2. \tag{15}$$

Using the Fourier transform of the top-hat beam $a_T(\kappa)$ as given in Eq. (13) gives

$$I(\rho = 0, \zeta) \approx \frac{\pi \rho_0^2}{2\zeta^3} \left| \frac{\zeta}{\rho_0} J_1\left(\frac{\rho_0}{\zeta}\right) \right|^2 = \frac{\pi}{2\zeta} \left| J_1\left(\frac{\rho_0}{\zeta}\right) \right|^2. \tag{16}$$

It will now be useful to use the following approximation for a vth order Bessel function of the first kind, which is valid when $x \gg 1$:

$$J_v(x) \approx \sqrt{\frac{2}{\pi x}} \cos\left(x - \frac{\pi}{4} - \frac{v\pi}{2}\right), \qquad x \gg 1, \tag{17}$$

$$\rightarrow J_1\left(\frac{\rho_0}{\zeta}\right) \approx \sqrt{\frac{2\zeta}{\pi \rho_0}} \cos\left(\frac{\rho_0}{\zeta} - \frac{3\pi}{4}\right), \qquad \zeta \ll \rho_0. \tag{18}$$

$$\Rightarrow I(\rho = 0, \zeta) \approx \frac{\pi}{2\zeta} \frac{2\zeta}{\pi \rho_0} \cos^2\left(\frac{\rho_0}{\zeta} - \frac{3\pi}{4}\right) = \frac{1}{\rho_0} \cos^2\left(\frac{\rho_0}{\zeta} - \frac{3\pi}{4}\right). \tag{19}$$

The form of the expression obtained in Eq. (19) brings us to an interesting conclusion—since ζ does not appear in the factor before the oscillatory $\cos^2$ term, the intensity of the maxima along $\rho = 0$ is constant when $\zeta \ll \rho_0$. Furthermore, we may now find the extrema of the function by taking the derivative and finding the values of ζ for which we get zero:

$$\frac{\partial}{\partial \zeta} I(\rho = 0, \zeta) = \frac{2}{\zeta^2} \cos\left(\frac{\rho_0}{\zeta} + \frac{\pi}{4}\right) \sin\left(\frac{\rho_0}{\zeta} + \frac{\pi}{4}\right) = 0, \tag{20}$$

$$\Rightarrow \zeta_\pm = \frac{\rho_0}{\pi\left(n \pm \frac{1}{4}\right)}, \qquad n \in \mathbb{Z}^+. \tag{21}$$

A simple calculation taking the derivative of Eq. (20) shows that ζ_- corresponds to local maxima, while ζ_+ corresponds to local minima. Examining Eq. (21) reveals that as $n \rightarrow \infty$ with $\zeta \rightarrow 0$, the separation between adjacent $\zeta_\pm$ values decreases at approximately the rate of $1/n^2$. This means the intensity along $\rho = 0$ is an oscillatory function whose frequency increases rapidly as $\zeta \rightarrow 0$. This feature suggests these beams may be used in super-resolution lensing [17], where high transverse wavevector components generate the intensity maxima in the region close to $\zeta = 0$. Further work is anticipated in this potential application.

When ζ is of the order of ρ_0, the approximation in Eq. (18) breaks down and instead we must examine Eq. (16) to find that as $\zeta \rightarrow \infty$ the intensity along $\rho = 0$ trails off slowly to zero since $J_1(\rho_0/\infty) = J_1(0) = 0$.

5. Conclusion

The structure of conically diffracted light was shown to depend sensitively on the profile of the incoming beam with a very clear difference between the intensity distribution formed when using a Gaussian input beam and when using a top-hat input beam. In particular, the interesting beam profile predicted to occur at the FIP for a top-hat input beam was compared to experimental observations and found to match well when taking into account the physical limitations of

the apparatus. The use of a variable iris to continuously vary the maximum transverse wavevector component of the beam allowed very fine control of the features of the intensity profile, such as the width of the high-intensity inner ring, and the relative intensities of the inner ring and the wedge-shaped feature. The evolution of such a beam beyond the FIP was simulated using the theoretical model presented which yielded the unusual feature of an oscillating axial spike. This evolution was then observed experimentally and found to match extremely well with the prediction.

This unusual intensity profile may find applications in optical trapping since the strength of a trap depends on the gradient of the intensity [18]. Since in theory the intensity of the inner ring is limited by the apparatus being used, the use of high-quality components could lead to a very stiff trap indeed. It may also be used to create microstructures with very sharp features, or controlled using a variable iris as described in Section 3 to produce microstructures with tunable feature quality. We also anticipate further work using white light top-hat beams to generate novel polychromatic beam shapes, and to perform experiments in cascade conical diffraction [19] and the generation of Bessel beams [20] in order to compare the results with the case of conically diffracted Gaussian beams.